Research Article Vol. 34, No. 8 / 20 Apr 2026 / Optics Express 14185
Optics EXPRESS

Leveraging low index contrast to reduce the polarization anisotropy in one-dimensional photonic crystals

JONATHAN BAROLAK,[1,4] AGOSTINO OCCHICONE,[2] FRANCESCO MICHELOTTI,[2] MARCO FINAZZI,[3] PAOLO BIAGIONI,[3] AND GIOVANNI PELLEGRINI[1,5]

[1]*Dipartimento di Fisica, Università degli Studi di Pavia, Via Bassi 6, 27100 Pavia, Italy*
[2]*Dipartimento di Scienze di Base e Applicate per l'Ingegneria, Sapienza Università di Roma, Via A. Scarpa 16, 00161 Roma, Italy*
[3]*Dipartimento di Fisica, Politecnico di Milano, Piazza Leonardo da Vinci 32, 20133 Milano, Italy*
[4]*jjbarolak@gmail.com*
[5]*giovanni.pellegrini@unipv.it*

Abstract: One-dimensional photonic crystals (1DPCs) are widely used optical platforms for guiding, filtering, and enhancing light at the nanoscale. Traditionally, designs have favored high refractive index contrast to maximize the size of the photonic band gap. Here, we demonstrate that low index contrast systems offer a powerful and underexplored route to achieving improved optical functionalities in truncated 1DPCs. In particular, we show that these systems enable closely aligned photonic band structures for transverse electric/magnetic (TE/TM) polarizations, allowing for broadband superposition of TE/TM Bloch surface waves (BSWs). As a demonstration of this approach, we design 1DPCs capable of generating planar superchiral fields, which require simultaneous excitation of TE/TM BSWs, for enhanced circular dichroism spectroscopy. To design such structures, we introduce an automated framework based on multi-objective genetic optimization. Comparing optimized designs in both high and low index contrast regimes, we find the low index contrast systems yield significantly larger optical chirality across the operational bandwidth due to the greater overlap between TE/TM BSW dispersion relations and the pronounced reduction in optical anisotropy. Furthermore, numerical simulations reveal that low index contrast structures offer improved robustness to fabrication tolerances and support a wider range of chiral analyte concentrations. In addition to their optical performance advantages, low index contrast systems are naturally compatible with polymeric materials, which offer benefits such as low cost, environmental sustainability, and mechanical flexibility. While this work focuses on surface wave behavior, the underlying design principle has broad implications for polarization-independent photonic technologies, including optical sensing, computing, and spectral filtering.

1. Introduction

Photonic crystals are foundational elements in nanophotonics, offering precise control over light propagation, confinement, and spectral/angular filtering through engineered periodic dielectric structures [1–3]. The simplest version is the one dimensional photonic crystal (1DPC) which has alternating planar layers of low- and high-refractive index materials. Although nomenclature varies across the literature, in this article we use the term 1DPC to refer to structures that may or may not exhibit periodicity in their layer thicknesses. 1DPCs have found widespread use due to their simplicity and versatility in applications ranging from biosensing and waveguiding to topological photonics with uses in optical communications, optical switching, and photonic integrated circuits [4–6]. In all application areas, the propagation of light through the 1DPC is

#585917 https://doi.org/10.1364/OE.585917
Journal © 2026 Received 9 Dec 2025; revised 11 Feb 2026; accepted 4 Mar 2026; published 7 Apr 2026

Optics EXPRESS

governed by the device's photonic band structure, the optical analogy to the electronic band structure in crystalline semiconductors, and the associated photonic bandgap (PBG) [7]. A strong trend in the photonic crystals community is to prefer 1DPC designs with large PBGs as they generally lead to better light control over a larger band of photon energies, have higher reflectivity coefficients, and stronger mode confinement [8–11]. The trend is so strong that there is a substantial push in the community to increase the dielectric contrast of organic materials to bring their advantageous characteristics, such as low production cost, ease to scale-up, elasticity, and potential to use recycled materials [10,12], to photonic crystal devices [13]. Though the design paradigm utilizing high index contrast devices has become a proven strategy for effective creation of 1DPC devices in applications such as reflectors, filters, and resonant optical structures, a new design challenge has arisen for 1DPCs requiring polarization independent behavior.

Light entering a 1DPC can be decomposed into two orthogonal polarization states: transverse electric (TE) and transverse magnetic (TM). The propagation of these two polarization states through a 1DPC is inherently different due to the optical anisotropy of the multilayer structure. The Brewster angle, where TM-polarized light is perfectly transmitted across an interface, is one prominent origin of such anisotropy [4,14]. Recently, however, there has been growing interest in polarization-independent filtering for optical computing, as well as polarization-independent surface state generation for superchiral light creation and multiplexed refractometric sensing using both polarization states [15–23]. Although these applications can often operate in angular and spectral regions away from the Brewster angle, where closer alignment of the TE and TM PBGs may be possible, the design of such polarization-independent 1DPCs remains a challenge. While low-index contrast systems have generally been overlooked due to their weaker confinement and narrower PBGs, they represent a largely untapped design space with unique optical properties.

In this work, we demonstrate that low-index contrast 1DPCs offer a powerful route to achieving novel optical functionalities through the close alignment of the TE and TM photonic band gaps. We explicitly show how utilizing such a design approach allows for broadband superposition of TE and TM Bloch Surface Waves (BSWs) for the generation of planar superchiral light fields [24]. Furthermore, we show how this design paradigm leads to 1DPC structures with reduced anisotropy in the confined fields leading to an enhanced optical chirality at the surface. The resulting surface waves have an almost circular polarization state, given equal input power between TE and TM modes, in contrast with previous works that predicted a strong ellipticity using high index contrast 1DPCs [18–21]. To design such structures, we develop a multi-objective genetic optimization framework that identifies layer thicknesses which support TE–TM mode overlap across a targeted spectral range. We compare designs in both a low and high index contrast regime and show that, owing to the consistent modal alignment and reduced anisotropy, the low-contrast designs (i) improve the generation of planar superchiral fields, (ii) exhibit enhanced robustness to fabrication tolerances, and (iii) support a broader operating range for chiral analyte detection. Beyond chiral sensing, the underlying principle, polarization mode alignment through low index contrast design, has broader implications for polarization independent photonic technologies. The compatibility of low-contrast designs with flexible, cost-effective, and environmentally friendly polymeric materials further expands their potential in scalable photonic systems, including spectral filtering, optical information processing, and integrated photonic circuits.

2. Results and discussion

Chirality is a fundamental property of matter in which an object's mirror image is not superimposable with itself despite being chemically identical. Chiral compounds are prolifically found in biological systems and pharmaceuticals where appropriately identifying the "handedness" of the compound is crucial for safe and effective treatment [25]. Optical diagnostic techniques, such as circular dichroism (CD) spectroscopy where the differential absorption between left and right hand circularly polarized light is measured, are commonly used for accurate identification of the

Optics EXPRESS

handedness of chiral matter due to the relatively simple optical setup, fast data collection and processing times, and nondestructive nature. However, CD signals are typically much weaker than standard absorption spectroscopies thus posing a challenge for measuring small concentrations of chiral analytes. To increase the light - chiral matter interaction, many solutions are coming forth which tailor the properties of the light field itself [26–30]. Typically this is achieved by increasing the optical chirality, which can be defined in free space as:

$$C = -\frac{\epsilon_0 \omega}{2} \mathrm{Im}\left(\mathbf{E}^* \cdot \mathbf{B}\right) \tag{1}$$

with ϵ_0 being the free space permittivity and ω being the optical angular frequency [31]. Circularly polarized light has an optical chirality of $C_{\mathrm{CPL}} = \pm\epsilon_0\omega/2$ and light with an optical chirality $C > C_{\mathrm{CPL}}$ would be considered superchiral. Most nanophotonic solutions are based on the idea of increasing the field confinement and thus increasing the absolute value of **E** and/or **B** while maintaining a phase factor and polarization that sustains an elliptical, or ideally circular, polarized light state. It remains a challenge, however, to produce light with high optical chirality factors over a uniform surface, which can easily be switchable between left and right hand polarization, and which works from near-UV to IR wavelength ranges where chiral spectroscopy is critical [32]. BSWs have recently been predicted to generate planar superchiral light fields by confining light at the surface for both polarization states simultaneously [18]. BSWs are excited by illuminating a truncated 1DPC at an angle and frequency such that the incident light is confined by total internal reflection at the external interface, while propagation into the multilayer is prohibited by the PBG, resulting in a surface-bound mode [8,33]. A qualitative field profile of a BSW is depicted in Fig. 1 and simulated BSW field profiles are shown in Fig. 3.

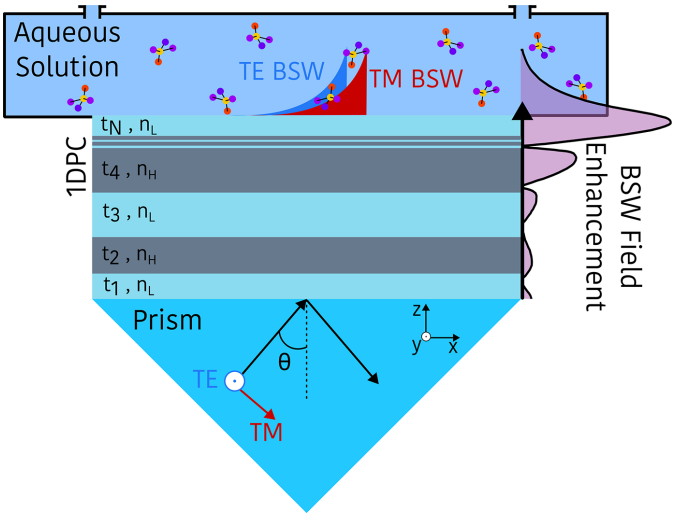

Fig. 1. A diagram of a 1DPC for simultaneous excitation of TE and TM mode Bloch surface waves. The system is designed in the Kretschmann configuration with a BK7 prism as the substrate and an aqueous solution where the chiral analytes would exist as the superstrate. The light blue layers of the 1DPC represent the low refractive index material (with refractive index n_L) and the gray layers represent the high refractive index material (with refractive index n_H). Here t_i represents the thickness of the i^{th} layer of the 1DPC.

An experimental apparatus for the excitation of superchiral fields is presented in Fig. 1. The system uses the Kretschmann configuration to ensure that the incident light field is under the total internal reflection condition at the top surface of the 1DPC [34]. Light, containing both TE and TM polarization states with the appropriate phase offset, enters the 1DPC at an oblique

Optics EXPRESS

angle from an N-BK7 glass prism. The fields propagate through the crystal and a strong field enhancement occurs at the top surface, which is an aqueous solution where the chiral analytes would exist during CD spectroscopy. To generate the largest optical chirality at the surface, we want to generate a structure which sustains BSW modes for both TE and TM polarization states at the same energy and momentum combination. To generate a large optical chirality over a range of wavelengths, which is required for CD spectroscopy, the dispersion relations of the TE and TM BSWs must be overlapped. Overlapping TE and TM BSW modes is a challenging design criteria for 1DPCs. Previous attempts have aimed at utilizing a "defect layer" at the termination of the 1DPC to align the dispersion relations of the BSWs, however this method comes at the price of a strong anisotropy [18–21]. Due to the anisotropy, the TM BSW was significantly weaker than the TE BSW, leading to a strong elliptical polarization state at the surface, given equal power in the two polarization states as input, and a non-ideal optical chirality. To maximize the optical chirality at the surface we developed an automated design method using genetic optimization.

2.1. Automated design of 1DPC structures

Optimization of photonic crystal structures is a challenge due to the rough solution space and the large dimensionality of the problem, especially when the constraint of a strict periodicity is relaxed. While gradient based optimization methods struggle in these conditions, genetic algorithms, methods developed by mimicking the natural selection and genetic crossing/mutation in biological evolution, have been shown to excel [35,36]. We use a genetic optimization method, specifically the Non-dominated Sorting Genetic Algorithm II (NSGA-II), with the aim to maximize the optical chirality generated at the top of our photonic crystal structure by optimizing the thicknesses of each layer within the 1DPC and the excitation angle of the light [37,38]. Our parameter vector is thus defined as:

$$\vec{x}_{\text{opt}} : [t_1, t_2, \ldots, t_N, \theta_1, \theta_2] \tag{2}$$

where t_i is the i^{th} layer thickness and $\theta_{1,2}$ are the excitation angles for the two wavelengths of light which define the desired operational spectral range of the system. To properly align the dispersion relations of the TE and TM BSW modes over a range of wavelengths, a single objective function is not sufficient as the dispersion relations could cross in (λ, θ) space providing a 1DPC with a large optical chirality at only a single wavelength. For proper dispersion alignment of the BSW modes, we utilized a two-objective optimization method which aimed at overlapping the dispersion relations at the two extremes of the wavelength range of interest. Though the TE and TM BSW dispersion relations can have different curvatures resulting in misaligned dispersion relations even when the BSW modes are overlapped at λ_1 and λ_2, we are investigating a relatively small energy-momentum space where the dispersion relations are somewhat linear. Therefore, we can attempt to align the dispersion relations by writing an automated design method that aims to overlap the two modes at the wavelength extremes. The evaluation functions thus are defined as:

$$\text{Eval} : [\frac{C_{\lambda_1}(z_s + z_0)}{C_{\text{CPL}}}, \frac{C_{\lambda_2}(z_s + z_0)}{C_{\text{CPL}}}] \tag{3}$$

where C_{λ_1} is the optical chirality at wavelength λ_1, z_s is the axial location of the top surface of the photonic crystal, and z_0 is some offset distance to calculate the optical chirality within the aqueous solution where the chiral compounds would exist in the experimental setup. The optical chirality for each individual within the species are calculated by simulating the electric and magnetic fields within the proposed design from each individual. The simulated fields are calculated using a rigorous coupled wave analysis (RCWA) approach with only a single Fourier harmonic taken to force lateral isotropy within the layers [39–41]. Plane wave solutions are assumed, and the field is calculated assuming incident illumination at both λ_1 and λ_2, with their associated incident angles taken from the values in the parameter vector for the given individual

Optics EXPRESS

within the population. Incident fields are assumed to have both polarization states present and the appropriate phase offset is calculated by maximizing the optical chirality at the distance z_0 above the top surface of the 1DPC for each individual.

As with all multi-objective optimization approaches, after the algorithm runs for many hundreds of generations a single optimized result is not generated but rather a line of "Pareto optimal" results forms in the $(\text{Eval}_1, \text{Eval}_2)$ solution space [42]. A Pareto optimal individual represents an optimized design which cannot be improved with respect to Eval_1 without coming at the cost of Eval_2 and vice versa. The collection of Pareto optimal solutions forms a so called "Pareto front". An example Pareto front is shown in Fig. 2. In this paper, we chose the Pareto optimal solutions whose evaluation functions summed together are maximal as our optimal solution.

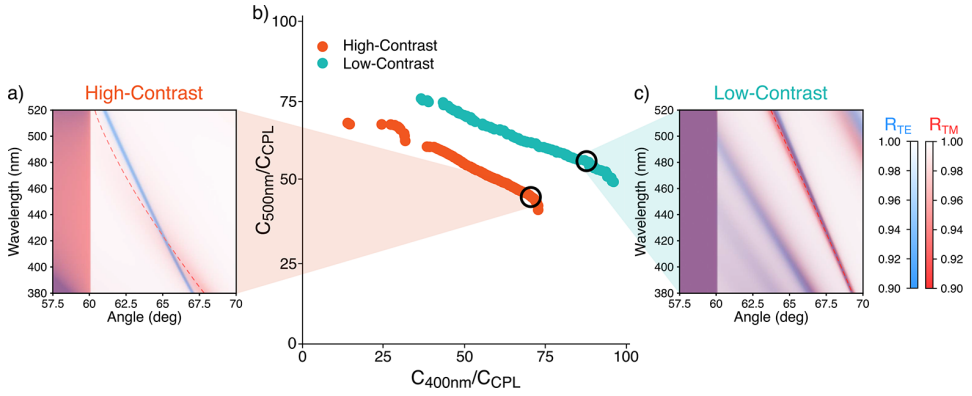

Fig. 2. Pareto fronts from a multi-objective optimization run with both a high and low index contrast system are presented in (b). In these optimizations, the thicknesses of a 1DPC were tailored to optimize the optical chirality enhancement at two different wavelengths. Reflectivity maps of one of the optimized designs from the high and low index contrast designs are presented in (a) and (c) with TE and TM modes being plotted in blue and red respectively. Dashed red lines are included to easily see the maximum of the TM BSW mode at each wavelength.

2.2. *Comparison of high and low index contrast optimized designs*

Two of the free parameters we have while using our genetic optimization method is the choice of materials for the high and low refractive index. The material choice, and thus the refractive index contrast, will have a strong impact on the photonic band structure and thus it makes sense to choose a refractive index contrast that will best align the photonic band structure for the two polarization states. We can evaluate how the refractive index contrast affects the propagation between the two polarization states by using the ubiquitous transfer matrix method, which relates the forward and backward propagating waves at one layer of a 1DPC to the forward and backward propagating waves at another layer [24]. This is done by assuming a plane wave solution to the electric field with amplitudes $E_{f,i}$ and $E_{b,i}$ for the forward and backward propagating waves in layer i which can be expressed as the vector $\begin{pmatrix} E_{f,i} \\ E_{b,i} \end{pmatrix}$. By calculating the transfer matrix $\mathbf{M}$ one can calculate the field in the next layer through: $\begin{pmatrix} E_{f,i+1} \\ E_{b,i+1} \end{pmatrix} = \mathbf{M} \begin{pmatrix} E_{f,i} \\ E_{b,i} \end{pmatrix}$. Due to linearity, this process can be repeated to calculate the field at any location within the crystal by multiplying together

Optics EXPRESS

the transfer matrices of subsequent layers:

$$\mathbf{M} = \prod_{i}^{I} \mathbf{M}_i = \left[\prod_{i}^{I} \mathbf{B}_{i-1,i} \mathbf{P}_i \right] \mathbf{B}_{I,I+1} \tag{4}$$

where $\mathbf{B}_{i-1,i}$ is the boundary matrix between the $(i-1)^{th}$ and i^{th} layer, with I being the total number of layers, and $\mathbf{P}_i$ is the propagation matrix within the i^{th} layer [43]. While the propagation matrices don't depend on the polarization state, the boundary matrix does depend on the polarization state since the reflectance and transmittance through a discontinuity in the refractive index depends on the polarization state of the incident light. The boundary matrices are given by:

$$\mathbf{B}_{i,i+1} = \frac{1}{2} \begin{pmatrix} 1 + \eta_{TE,TM} & 1 - \eta_{TE,TM} \\ 1 - \eta_{TE,TM} & 1 + \eta_{TE,TM} \end{pmatrix} \tag{5}$$

where the $\eta_{TE,TM}$ parameters can be related to each other through:

$$\eta_{TM} = \frac{n_i^2}{n_{i+1}^2} \eta_{TE}. \tag{6}$$

Investigating Eq. (6), a natural choice in materials arises when trying to align dispersion relations between the TE and TM modes. Since the band diagrams are going to be intimately related to the equations relating the propagation of waves across the boundaries within the photonic crystal, it makes sense that we should choose materials that minimize the dissimilarity between the transfer matrices for the 1DPC of both polarization states. As one can see, the only difference in the transfer matrix for the two polarization states is the $\eta_{TE,TM}$ parameter in Eq. (6) which is minimized when $|n_i^2/n_{i+1}^2 - 1|$ is at a minimum. Therefore, choosing two materials with a low index contrast should result in more similar band structures as compared to materials with a larger refractive index contrast.

To see whether the physical intuition of using a low index contrast design allows for improved overlap of the TE and TM BSWs, genetic optimization runs were performed using both design philosophies. To ensure a fair comparison, the optimization parameters were held constant, including the crossover probability, which governs the rate at which parent solutions are recombined, and the clustering parameter, which sets the minimum distance required between individuals to prevent excessive crowding around a single solution [37]. Each optimization run had 300 generations with 300 individuals in each generation. The evaluation functions optimized the optical chirality at a position $z_0 = 5$ nm above the surface of the top layer for $\lambda_1 = 400$ nm and $\lambda_2 = 500$ nm.

Because high-index contrast designs inherently enlarge the photonic band gap, they yield stronger TE BSW confinement and thus they can support BSW modes with a larger optical chirality for a given number of layers than the low-index contrast designs (see Supplement 1, "Effect of Refractive Index Contrast on Field Confinement") [44]. However, the achievable enhancement is ultimately limited by the finite angular resolution of coupling optics, so further narrowing of the resonance beyond this limit does not provide an experimental advantage. Moreover, since our designs employ relatively few layers, fabricating additional layers does not represent a practical constraint, whereas maintaining experimentally accessible modal widths is essential. For this reason, we define a fair comparison between the two optimized designs as one in which the TE BSWs exhibit equal angular width, even if this requires a different number of layers in each case. The TE polarization state is used for this comparison because polarization anisotropy in the relevant spectral and angular range broadens the TM mode, which makes the TE angular width the experimentally limiting factor for achievable large optical chirality.

Optics EXPRESS

Optimizations were performed for a 1DPC with $n_L = 1.50$ and $n_H = 1.60$ for the low index contrast design and $n_L = 1.50$ and $n_H = 2.55$ for the high index contrast design. These refractive index values were chosen to strike a balance between being close to the values of real world materials (such as the polystyrene, cellulose, SiO_2, and Ta_2O_5 which are used in the Supplement 1 demonstration with dispersive materials) while maintaining the same refractive index value for the low index material [45–48]. The extinction coefficient was held constant at $k = 0.0001$ for all layers, chosen to be similar to SiO_2 and Ta_2O_5 in the wavelength range of interest, excluding the water superstrate and the glass substrate which contained no absorption [49]. Since the exact k values can drastically differ with optical quality, surface roughness, and temperature, an analysis on the effect of the absorption value on these results is presented in the section "Effect of Absorption within the 1DPC" in Supplement 1. To utilize the optimization method for the purpose of determining which design paradigm is preferable, material dispersion was not taken into account. However, results between materials with dispersion taken into account are presented in the section "Optimization with Dispersive Materials" in Supplement 1 and the same findings are displayed in those optimizations. The high index contrast design was optimized with 5 layers of alternating low and high index material with the low index materials being the initial and final layers of the 1DPC. The low index contrast design had the same functional form but contained 13 layers. Fine tuning of the high refractive index value, n_H, was used to ensure the modal thicknesses were identical between the low and high index designs.

Results from the two-objective, genetic optimizations for both the high and low contrast design strategies are presented in Fig. 2. The individuals plotted in $(\text{Eval}_1, \text{Eval}_2)$ space represent the individuals of the Pareto front of the last generation of the genetic optimization. The shapes of the Pareto fronts are similar, however the low-contrast Pareto front fully dominates the high contrast Pareto front. This means that for every design on the high-contrast Pareto front, there exists a corresponding design on the low-contrast Pareto front that achieves equal or better chirality enhancement in both objectives, and strictly better in at least one. To gain a better sense for what is causing this improvement, we can plot the reflectivity maps in (λ, θ) space for the individuals in each Pareto front which maximize the sum of the individual's optical chirality enhancement values at the two wavelength extremes [50]. The details on these optimized structures are reported in the section "Optimized 1DPC Designs" in Supplement 1. The reflectivity maps for these designs are plotted in Fig. 2 where the red hue represents the reflectivity of the TM mode and the blue hue represents the reflectivity of the TE mode. Due to the broad BSW resonance of the TM mode for the high-contrast design, a dashed line is plotted to show the angle of the minimum reflectivity dip for each wavelength. The reflectivity maps indicate that the improved optical chirality performance in the low-contrast design is caused by an increase in the modal overlap and a reduced anisotropy. Specifically from the dashed lines, it is clear that the TE and TM BSW dispersion relations are well aligned, being almost completely overlapped, in the low-contrast while in the high-contrast case they both exhibit different line shapes and remain non-superimposed except for a single crossing point. Additionally, we see a significant decrease in anisotropy in the low contrast design due to narrow TM BSW mode as compared to the broad TM BSW mode in the high contrast design.

The reflectivity map of the low-contrast optimized design in Fig. 2 shows multiple modes directly adjacent to the BSW mode, highlighting the significantly smaller PBG compared to the high-contrast design. To confirm that we are indeed observing the BSW mode instead of guided modes, we plot the field amplitudes $|E_x(z)|$ and $|H_x(z)|$, along with the optical chirality enhancement $C_{\lambda_1}(z)/C_{CPL}$, as functions of the axial distance z through the 1DPC. The fields are calculated at $\lambda = 400$ nm and $\theta_{inc} = \theta_{400}$ where θ_{400} is the angle which maximizes the optical chirality at 400 nm for each design respectively. The x components of the electric and magnetic fields for the optimized high and low index contrast designs are plotted in Fig. 3. Here the fields are normalized to the amplitude of the incoming field. The y and z components of the fields are

Optics EXPRESS

plotted in Supplement 1. The index profiles are shown in gray in the background. In the substrate, we see the interference between the forward and backward propagating plane waves giving rise to a stationary field. Tracking the field amplitude of the low contrast design, we see an exponential increase of the local field maxima inside the 1DPC followed by the expected exponential decay in the superstrate. This behavior shows that the investigated mode in the reflectivity map is indeed a BSW and not a guided mode. Additionally, in the field profiles, it is clear to see the reduced anisotropy in the low contrast design. Comparing the field of the TE and TM modes in the superstrate, we see almost identical enhancements showing that the surface wave has an almost perfectly circular polarization (when phased delayed by $\pi/2$ with respect to one another) while the high contrast design has strong ellipticity. The chirality enhancement as a function of axial distance are also plotted in Fig. 3.

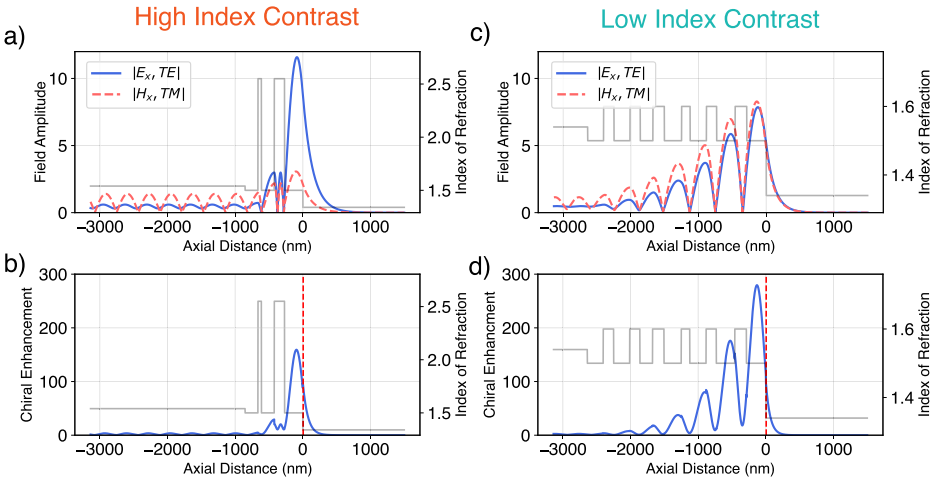

Fig. 3. Axial field amplitude profiles, for only x field components, are shown for the high and low index contrast designs in (a) and (c) for a plane wave launched at the angle which optimizes the strength of the BSW for light with $\lambda = 400$ nm. Axial optical chirality enhancement profiles are presented in (b) and (d) with the red dashed line representing the axial point z_0 where the optical chirality is calculated for the genetic algorithm's evaluation functions.

To assess the optical chirality performance throughout the entire operation wavelength range, we can plot the map of the optical chirality in (λ, θ) space. The resulting chirality maps, calculated at $z = z_0$ above the surface of the 1DPC, are shown in Fig. 4(b) and (c). Here the chirality values are calculated with the optimized phase offset for λ and θ_{inc} within the map. We see in the low contrast chirality map, the guided modes have significantly lower optical chirality at the surface as compared to the BSW mode likely because their field distributions have localized field enhancement contained within the layers of the 1DPC instead of at the surface. The chirality maps show that the strongest superchiral light at the surface of the 1DPC is only generated when the TE and TM BSW modes are overlapped in (λ, θ) space. Running along the dispersion relations of both chirality maps, we can plot the maximum optical chirality as a function of angle for each wavelength. Plotted in Fig. 4(a) we see the optical chirality at every wavelength is improved for the low contrast design as compared to the high contrast design.

2.3. *Modal width analysis*

To make the fairness of the comparison between the two designs explicit, we examine the angular widths of the BSWs. Figure 5(a) and (c) plot the normalized optical chirality, while panels (b) and

Optics EXPRESS

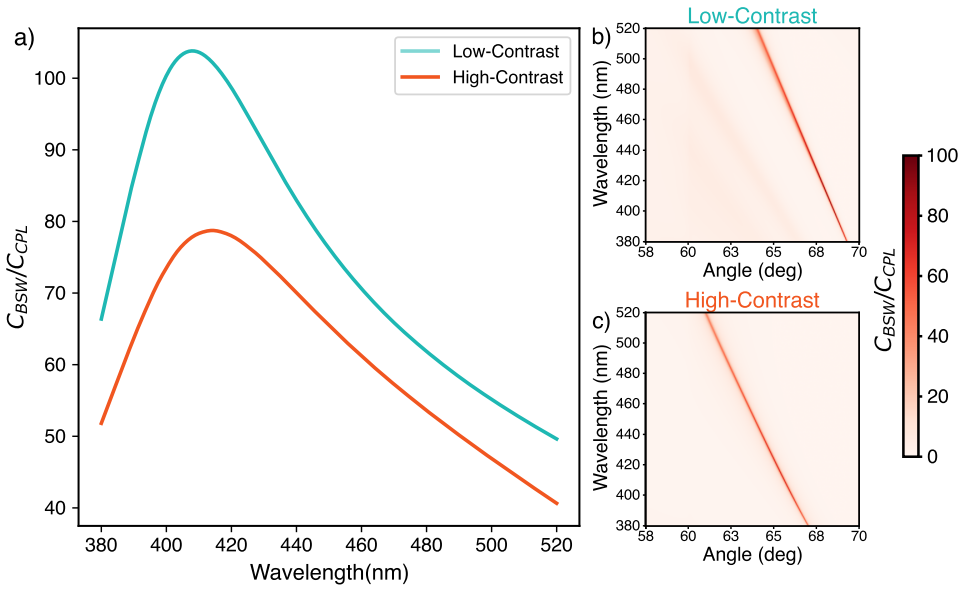

Fig. 4. The optical chirality enhancement value is plotted in (a) for both the high and low contrast designs over the entire operational bandwidth. The associated chirality maps are presented in (b) and (c).

(d) plot the TE mode reflectivity. To assess the modal widths, the reflectivity spectra of the TE BSW is plotted for various horizontal lineouts of the reflectivity map shown in Fig. 2 for several wavelengths over the operational wavelength range. The minima have been centered for ease of comparison. The angular reflectivity spectra are colored on a linear color map which varies from blue to red as the wavelength ranges from 400 nm to 500 nm. Dashed lines are included to show the average FWHM over the entire wavelength range. The average angular FWHM for the low contrast TE reflectivity dip is 67 mdeg and 66 mdeg for the high index contrast design, confirming the validity of the comparison. The width of the TE BSW reflectivity dip was chosen as the criterion for comparison, rather than the width of the chirality enhancement, because the latter depends on both the modal widths of the TE and TM BSWs as well as their relative overlap. The TE BSW width, which is typically narrower than that of the TM BSW due to the larger PBG, provides a more direct measure of resonance sharpness and field confinement. Nonetheless, calculating the width of the chirality enhancement remains useful, as it specifies the angular range over which the resonant mode can be experimentally coupled. Here we again see similar FWHM for the two designs with the low contrast having a FWHM of 120 mdeg and the high contrast having a FWHM of 110 mdeg. An increased optical chirality enhancement would be expected for 1DPCs supporting narrower resonances, however these systems would require an experimental system with improved angular uncertainty in order to take advantage of such a narrow resonance.

2.4. *Stability analysis*

In this section the effect of two sources of experimental instability are analyzed for the optimized 1DPCs from the high and low index contrast paradigms. The first source of instability can be ascribed to common manufacturing uncertainty. Though fabrication methodologies of 1DPCs have dramatically improved in recent decades, thickness uncertainties are still a prevalent problem in the manufacturing of high-Q 1DPCs. To investigate our designs' stability to manufacturing uncertainties in the thickness of the 1DPCs, Monte Carlo Uncertainty Analysis was performed on the optimized designs. To simulate the manufacturing defects, a 1DPC was simulated with

Optics EXPRESS

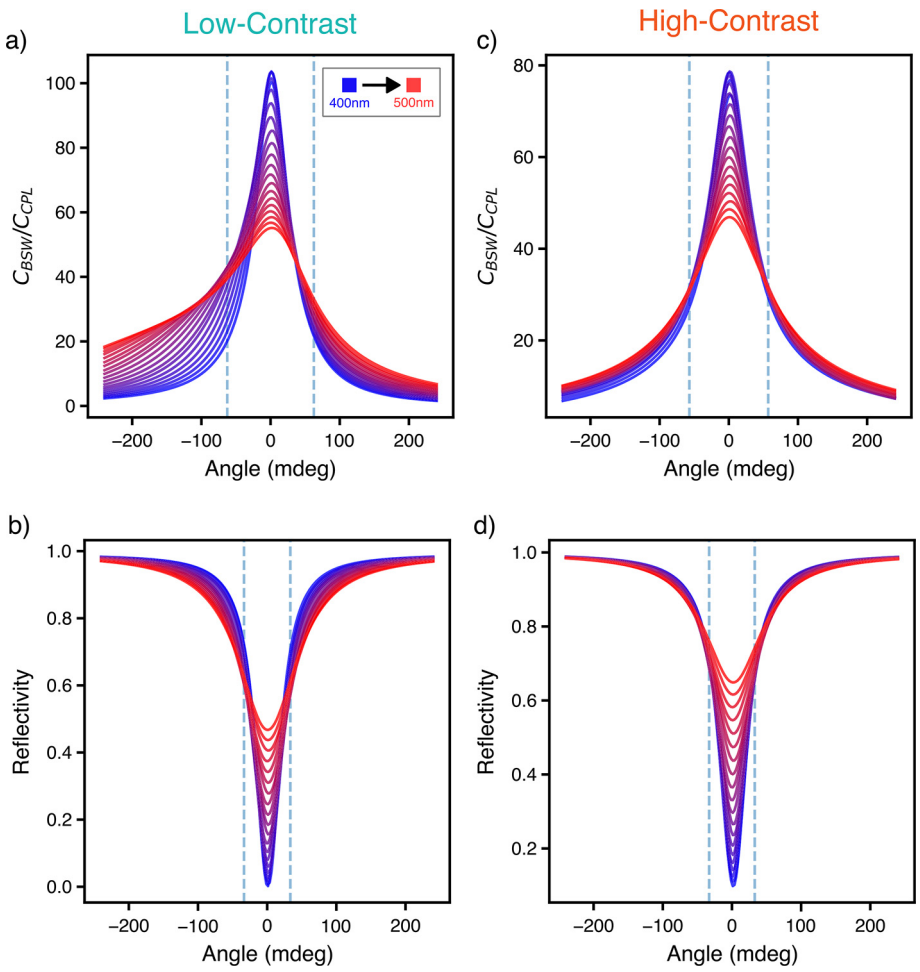

Fig. 5. The modal widths for the high and low index contrast designs are presented for both the TE reflectivity maps (b) and (d) as well as the optical chirality enhancement maps (a) and (c). The spectra are calculated for many wavelengths between 400 nm and 500 nm, which are colored accordingly from blue to red. Vertical dashed lines are included to show the average FWHM calculated over all lineouts for a given plot.

thicknesses chosen from a random normal distribution:

$$t_i \sim \mathcal{N}(\mu_i, \sigma^2) \quad \text{for } i = 1, \ldots, N \tag{7}$$

where t_i is the thickness of the i^{th} layer, $\mathcal{N}$ is the normal distribution function, μ_i is the actual thickness of the optimized design, and σ is the standard deviation which was set to 5 nm [51]. The optical chirality angular spectrum was calculated for the faulty design at both design wavelengths and the maximum chirality enhancement values were recorded such that resonant shifts did not artificially lower the performance of the sensor. This process is repeated for many hundreds of iterations to generate a distribution of optical chirality values for statistical analysis of the effect of the manufacturing uncertainties. A dataset of the faulty chirality enhancement values, normalized to the 'ideal' case, are presented in Fig. 6(a) and (b) for the low and high index contrast optimized designs. Here the optical chirality enhancement of the individual with the manufacturing defects at 400 nm are plotted in blue and at 500 nm are plotted in red. It can

Optics EXPRESS

easily be seen that the low index contrast designs are sizably more robust to uncertainties in the thickness despite the fact that there are more layers. The standard deviation for the normalized optical chirality enhancement is around 8% for the low contrast case and around 20% for the high contrast case. It may look surprising that there are enhancements to the optical chirality in both the low contrast and high contrast designs when the thicknesses are sampled from a random distribution centered around the optimized thicknesses. However, due to the multi-objective nature of the optimization approach, an enhancement in one design criterion can generally be made at the cost of the other criterion. A deeper analysis of this subject is presented in the section "Monte Carlo Uncertainty Analysis and Pareto Stability" in Supplement 1 [52]. This analysis shows that the low contrast design paradigm also leads to designs which are significantly more robust to manufacturing uncertainties than the standard high contrast designs.

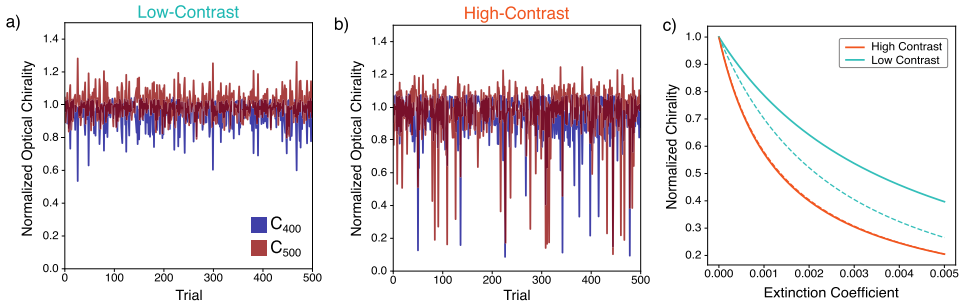

Fig. 6. (a) and (b) show the results of a Monte Carlo sensitivity analysis where many iterations of the 1DPC are generated with the thickness pulled from a random normal distribution with a standard deviation of 5 nm to simulate imperfections of the thickness in the manufacturing process. (c) shows the normalized optical chirality enhancement as a function of absorption coefficient in the aqueous superstrate. The optical chirality from each trial was calculated at both 400 nm, dashed line, and 500 nm, solid line, illumination wavelengths.

The second source of experimental instability is from absorption of the chiral analytes. The goal of generating superchiral light is to enhance the interaction of light with chiral media, thus lowering the required concentration in order to measure a detectable CD signal. Most of these techniques, including the 1DPCs, however work with relatively narrow resonances to generate the superchiral light which often require specific operating conditions for the resonance to be present. Absorption of the light in the region where the chiral analytes exist, for example, can disturb the resonance conditions. Thus these techniques typically bring with them a relatively small operating range of chiral analytes concentrations under which the superchiral light will exist. We can mimic this effect numerically by adding an absorbing layer on the top of our 1DPC sensor with a thickness of 1000 nm to act as our layer of chiral analytes. The index of refraction of this layer will be identical to water however the imaginary part of the refractive index will vary between $0.000 \leq k \leq 0.005$. At each absorption value, the optical chirality enhancement will be measured at the same point $z_0 = 5$ nm above the crystal, within the absorbing layer, as before. This was calculated using both the low index contrast and high index contrast design at both 400 nm and 500 nm. The chirality enhancement value, normalized to the case with no absorption, for each absorption value is displayed in the plot in Fig. 6(c). Here the dashed line represents the normalized optical chirality enhancement for 500 nm while the solid line represents the value for 400 nm illumination. We see that the optical chirality decreases significantly faster for the high index contrast case than for the low index contrast case. For 500 nm illumination, the high index contrast has reached 50% of its ideal optical chirality value for an extinction value of 0.001 while the low index contrast design doesn't reach this level until an absorption value of 3 times

Optics EXPRESS

that absorption value. This analysis shows that the low index contrast design also has a larger operational chiral analyte concentration range than the high index contrast design.

3. Conclusion

In this article, we showed how a low index contrast design approach can be used to achieve improved optical functionalities. Specifically, we showed how a 1DPC with a low index contrast design can be used to significantly improve the alignment of the band structure and reflectivity maps of TE and TM light waves in a truncated 1DPC. To show the utility of such a design paradigm, we presented a multi-objective genetic optimization algorithm for generating optimized 1DPCs with tailored thicknesses for producing superchiral light fields, a challenging inverse design problem which requires alignment of TE and TM BSW modes. The optimized designs were then compared to show that the low index contrast system generated designs with improved optical chirality over the entire wavelength range of interest. By investigating the fields within the optimized crystals and the reflectivity spectra, we saw that the low contrast designs had significantly improved overlap of the TE and TM BSW modes and a large reduction in the anisotropy of the fields confined to the surface. Through Monte Carlo stability analysis and numerical simulations of the absorption of the confined fields at the surface, we showed how the low contrast designs were significantly more robust to manufacturing uncertainties in the thicknesses of each layer and were capable of operating with a larger range of chiral analyte concentrations on top of the 1DPC. The results from this analysis not only represents a major improvement in generating experimentally viable planar superchiral fields for sensitive chiral spectroscopy techniques, but also presents an important new design paradigm for polarization-insensitive 1DPCs which could have major impacts in fields like optical computing, sensing, and filtering.

Funding. European Union-Next Generation EU-PNRR-M4C2, investimento 1.1-"Fondo PRIN 2022"-"SPIRAL – Lossless surface waves for chiral spectroscopy" (2022WFM5MZ – CUP F53D23001140001).

Acknowledgments. This work was partially funded by the European Union-Next Generation EU-PNRR-M4C2, investimento 1.1-"Fondo PRIN 2022"-"SPIRAL – Lossless surface waves for chiral spectroscopy" – id 2022WFM5MZ – CUP F53D23001140001.

Disclosures. The authors declare no conflicts of interest.

Data availability. Data underlying the results presented in this paper are not publicly available at this time but may be obtained from the authors upon reasonable request.

Supplemental document. See Supplement 1 for supporting content.

References

1. E. Yablonovitch, "Inhibited Spontaneous Emission in Solid-State Physics and electronics," Phys. Rev. Lett. **58**(20), 2059–2062 (1987).
2. S. John, "Strong localization of photons in certain disordered dielectric superlattices," Phys. Rev. Lett. **58**(23), 2486–2489 (1987).
3. R. K. Gangwar, A. K. Pathak, and S. Kumar, "Recent Progress in Photonic Crystal Devices and Their Applications: A review," Photonics **10**(11), 1199 (2023).
4. P. Li, Y. Guo, Y. Xi, *et al.*, "Controlling the TE-TM splitting of topological photonic interface states by precise incident angle adjustment," Commun. Phys. **7**(1), 201 (2024).
5. V. N. Konopsky and E. V. Alieva, "Photonic crystal surface waves for optical biosensors," Anal. Chem. **79**(12), 4729–4735 (2007).
6. E. Descrovi, F. Frascella, B. Sciacca, *et al.*, "Coupling of surface waves in highly defined one-dimensional porous silicon photonic crystals for gas sensing applications," Appl. Phys. Lett. **91**(24), 241109 (2007).
7. J. D. Joannopoulos, S. G. Johnson, J. N. Winn, *et al.*, *Photonic Crystals: Molding the Flow of Light* (Princeton University Press, 2008), 2nd ed.
8. D. Aurelio and M. Liscidini, "Electromagnetic field enhancement in Bloch surface waves," Phys. Rev. B **96**(4), 045308 (2017).
9. Y. Fink, J. N. Winn, S. Fan, *et al.*, "A dielectric omnidirectional reflector," Science **282**(5394), 1679–1682 (1998).
10. A. C. Edrington, A. M. Urbas, P. DeRege, *et al.*, "Polymer-based photonic crystals," Adv. Mater. **13**(6), 421–425 (2001).

Optics EXPRESS

11. M. Müller, R. Zentel, T. Maka, *et al.*, "Photonic Crystal Films with high refractive index contrast," Adv. Mater. **12**(20), 1499–1503 (2000).
12. P. Lova, H. Megahd, P. Stagnaro, *et al.*, "Strategies for Dielectric Contrast Enhancement in 1d planar polymeric photonic crystals," Appl. Sci. **10**(12), 4122 (2020).
13. L. Fornasari, F. Floris, M. Patrini, *et al.*, "Demonstration of fluorescence enhancement via Bloch surface waves in all-polymer multilayer structures," Phys. Chem. Chem. Phys. **18**(20), 14086–14093 (2016).
14. S.-G. Lee and R. Magnusson, "Essential differences between TE and TM band gaps in periodic films at the first Bragg condition," Opt. Lett. **44**(19), 4658 (2019).
15. W. Xue and O. D. Miller, "High-NA optical edge detection via optimized multilayer films," J. Opt. **23**(12), 125004 (2021).
16. X. Zhang, B. Bai, H.-B. Sun, *et al.*, "Incoherent Optoelectronic Differentiation Based on optimized multilayer films," Laser Photonics Rev. **16**(9), 2200038 (2022).
17. Y. Liu, M. Huang, Q. Chen, *et al.*, "Single planar photonic chip with tailored angular transmission for multiple-order analog spatial differentiator," Nat. Commun. **13**(1), 7944 (2022).
18. G. Pellegrini, M. Finazzi, M. Celebrano, *et al.*, "Chiral surface waves for enhanced circular dichroism," Phys. Rev. B **95**(24), 241402 (2017).
19. G. Pellegrini, M. Finazzi, M. Celebrano, *et al.*, "Surface-enhanced chiroptical spectroscopy with superchiral surface waves," Chirality **30**(7), 883–889 (2018).
20. G. Pellegrini, M. Finazzi, M. Celebrano, *et al.*, "Superchiral Surface Waves for all-optical enantiomer separation," J. Phys. Chem. C **123**(46), 28336–28342 (2019).
21. E. Mogni, G. Pellegrini, J. Gil-Rostra, *et al.*, "One-Dimensional Photonic Crystal for surface mode polarization control," Adv. Opt. Mater. **10**(21), 2200759 (2022).
22. G. Pitruzzello and T. F. Krauss, "Photonic crystal resonances for sensing and imaging," J. Opt. **20**(7), 073004 (2018).
23. T.-L. Guo, B. Fazlpour, M. Kuittinen, *et al.*, "Polarization-insensitive surface mode excitation on metamaterial-terminated one-dimensional photonic crystals," J. Phys. Photonics **7**(3), 035007 (2025).
24. P. Yeh, A. Yariv, and C.-S. Hong, "Electromagnetic propagation in periodic stratified media I General theory*," J. Opt. Soc. Am. **67**(4), 423 (1977).
25. P.-H. Chuong, L. A. Nguyen, H. He, *et al.*, "Chiral Drugs. an overview," Int. J. Biomed. Sci. **2**(2), 85–100 (2006).
26. M. L. Solomon, A. A. E. Saleh, L. V. Poulikakos, *et al.*, "Nanophotonic Platforms for Chiral Sensing and separation," Acc. Chem. Res. **53**(3), 588–598 (2020).
27. A. Biswas, P. Cencillo-Abad, M. W. Shabbir, *et al.*, "Tunable plasmonic superchiral light for ultrasensitive detection of chiral molecules," Sci. Adv. **10**(8), eadk2560 (2024).
28. E. Mohammadi and G. Tagliabue, "Nanophotonic-Enhanced Thermal Circular Dichroism for chiral sensing," ACS Photonics **12**(1), 152–158 (2025).
29. J. Mun, M. Kim, Y. Yang, *et al.*, "Electromagnetic chirality: From fundamentals to nontraditional chiroptical phenomena," Light: Sci. Appl. **9**(1), 139 (2020).
30. H. Ali, E. Petronijevic, G. Pellegrini, *et al.*, "Circular dichroism in a plasmonic array of elliptical nanoholes with square lattice," Opt. Express **31**(9), 14196 (2023).
31. Y. Tang and A. E. Cohen, "Optical Chirality and Its Interaction with matter," Phys. Rev. Lett. **104**(16), 163901 (2010).
32. M. Finazzi, P. Biagioni, M. Celebrano, *et al.*, "Quasistatic limit for plasmon-enhanced optical chirality," Phys. Rev. B **91**(19), 195427 (2015).
33. F. Michelotti, "Bloch surface waves on dielectric one-dimensional photonic crystals: Fundamental properties and applications," Opt. Mater. Express **15**(11), 2839 (2025).
34. A. Occhicone, M. Pea, R. Polito, *et al.*, "Spectral Characterization of Mid-Infrared Bloch Surface Waves Excited on a truncated 1d photonic crystal," ACS Photonics **8**(1), 350–359 (2021).
35. M. J. Safdari, S. M. Mirjalili, P. Bianucci, *et al.*, "Multi-objective optimization framework for designing photonic crystal sensors," Appl. Opt. **57**(8), 1950 (2018).
36. Y. Shi, W. Li, A. Raman, *et al.*, "Optimization of Multilayer Optical Films with a Memetic Algorithm and mixed integer programming," ACS Photonics **5**(3), 684–691 (2018).
37. K. Deb, A. Pratap, S. Agarwal, *et al.*, "A fast and elitist multiobjective genetic algorithm: Nsga-ii," IEEE Trans. Evol. Computat. **6**(2), 182–197 (2002).
38. F.-A. Fortin, F.-M. De Rainville, M.-A. Gardner, *et al.*, "DEAP: Evolutionary algorithms made easy," J. Machine Learning Research **13**, 2171–2175 (2012).
39. D. M. Whittaker and I. S. Culshaw, "Scattering-matrix treatment of patterned multilayer photonic structures," Phys. Rev. B **60**(4), 2610–2618 (1999).
40. B. Vial and Y. Hao, "Open-Source Computational Photonics with auto differentiable topology optimization," Mathematics **10**(20), 3912 (2022).
41. B. Vial, "nannos," (2022).
42. Y. Censor, "Pareto optimality in multiobjective problems," Appl. Math. Optim. **4**(1), 41–59 (1977).
43. M. Gryga, D. Ciprian, L. Gembalova, *et al.*, "Sensing based on Bloch surface wave and self-referenced guided mode resonances employing a one-dimensional photonic crystal," Opt. Express **29**(9), 12996 (2021).
44. A. Yariv and P. Yeh, *Optical Waves in Crystals* (Wiley Interscience, 1984).

Optics EXPRESS

45. L. Gao, F. Lemarchand, and M. Lequime, "Exploitation of multiple incidences spectrometric measurements for thin film reverse engineering," Opt. Express **20**(14), 15734 (2012).
46. N. Sultanova, S. Kasarova, and I. Nikolov, "Dispersion Properties of optical polymers," Acta Phys. Pol. A **116**(4), 585–587 (2009).
47. X. Zhang, J. Qiu, X. Li, *et al.*, "Complex refractive indices measurements of polymers in visible and near-infrared bands," Appl. Opt. **59**(8), 2337 (2020).
48. D. Franta, D. Nečas, I. Ohlídal, *et al.*, "Optical characterization of SiO_2 thin films using universal dispersion model over wide spectral range," in *Optical Micro- and Nanometrology VI*, vol. 9890 C. Gorecki, A. K. Asundi, and W. Osten, eds. (SPIE / International Society for Optics and Photonics, 2016), p. 989014.
49. D. Franta, J. Vohánka, J. Dvorák, *et al.*, "Wide spectral range optical characterization of tantalum pentoxide (ta_2o_5) films by the universal dispersion model," Opt. Mater. Express **15**(4), 903 (2025).
50. H. Wankerl, M. L. Stern, A. Mahdavi, *et al.*, "Parameterized reinforcement learning for optical system optimization," J. Phys. D: Appl. Phys. **54**(30), 305104 (2021).
51. A. Anopchenko, A. Occhicone, R. Rizzo, *et al.*, "Effect of thickness disorder on the performance of photonic crystal surface wave sensors," Opt. Express **24**(7), 7728 (2016).
52. J. Bader and E. Zitzler, "Hype: An algorithm for fast hypervolume-based many-objective optimization," Evol. Comput. **19**(1), 45–76 (2011).